Appl. Phys. B 71, 627–633 (2000) / Digital Object Identifier (DOI) 10.1007/s003400000386

Applied Physics B
Lasers
and Optics

Direct mapping of insertion reaction dynamics: $S(^1D) + H_2 \rightarrow SH + H$

S.-H. Lee, K. Liu

Institute of Atomic and Molecular Sciences (IAMS), Academia Sinica, Taipei, Taiwan 10764

Received: 26 February 2000/Revised version: 20 April 2000/Published online: 13 September 2000 –

Abstract. The Doppler-selected time-of-flight method was applied to map out the differential cross sections of the title reaction at two collision energies in a crossed-beam experiment. Roughly symmetric and highly forward–backward peaking angular distributions were observed at both energies. Vibrational structures of the SH product were resolved from the velocity measurements of the counter-product H-atom. Most of the angle-integrated observables can readily be understood on statistical grounds, which suggests that statistics plays the dominant role in determining the outcomes of this prototypical insertion reaction. In terms of more detailed angle-specific reaction attributes, significant discrepancies from statistical considerations were revealed, indicative of some hidden dynamics being buried under the statistical factor.

PACS: 30; 40; 80

Elementary atom–molecule reaction often proceeds by single-bond formation and single-bond breaking processes [1]. It can be of a direct abstraction or exchange type in which the formation of a new bond and the rupture of an old bond occur "simultaneously". Alternatively, it can be of an indirect type in which an intermediate complex is first formed by an end-on addition process and the product is subsequently produced by complex decomposition or an elimination process. In this case, these two processes can be regarded as two independent, sequential steps. Typical examples for these two mechanisms are reactions involving a uni-valent atom, such as that in its electronic P-state. There is, however, another important type of indirect reaction pathway – a side-on insertion. Insertion is characterized by a simultaneous one-bond rupture and two-bonds formation process in complex formation. It typically occurs for a divalent atom or radical, such as that in the electronic D-state. Either the addition–elimination or the insertion–decomposition mechanism involves an intermediate reaction complex, and the statistical treatment has often proven to be a powerful tool in rationalizing many of the experimental observations. The more detailed attributes, such as the roles of initial impact parameter and/or the angle of attack [2], the subtle dependence of the intramolecular isotope branching (for example, in the case of $X + HD$) on the PESs [3, 4] etc, however remain unclear.

There is now strong evidence that the reaction of a divalent $S(^1D)$ atom with H_2 proceeds almost exclusively via insertion mechanism at low collision energy [2, 4–6]. In view of the basic concept given above and the analogous, better-known reaction of $O(^1D) + H_2$, this conclusion is what one would have anticipated. The energetics of these two reactions are, however, sufficiently different so that the underlying reaction dynamics might not necessarily be the same. Figure 1 depicts the relevant energetics for the two reactions. Excitation function measurements for $O(^1D) + H_2$ [7] and $S(^1D) + H_2$ [4] at low energies indicate that both reactions are of capture type, namely their reactivities are governed by long-range attractive forces with little activation energy. The favored path for both reactions is thus believed to be insertion forming the reaction complexes H_2S and H_2O, respectively. The well depths of the reaction complexes in the two cases are quite comparable, 90 and 118 kcal/mol with respect to products, respectively. The exoergicity for the $S(^1D) + H_2$ reaction is, however, substantially smaller than that for $O(^1D) + H_2$, 6.9 versus 43.3 kcal/mol. Because of the deep potential well and the small exoergicity, conventional wisdom will then predict a long-lived complex (a few ps based on a simple RRKM prediction) being involved in the reaction of $S(^1D) + H_2$ and that the statistical behavior might prevail [1]. That is in constrast with a short-lived complex mechanism for the $O(^1D) + H_2$ reaction, for which both RRKM estimation and dynamics calculation [8] indicate that the complex survives only a few vibrational oscillations before decomposition.

In addition to the lowest energy ($1^1A'$) insertion pathway, the interactions of a ^1D-atom with H_2 lead to four other asymptotically degenerate potential energy surfaces (PESs). For $O(^1D) + H_2$ both experiment [7] and high-quality ab initio calculations [9, 10] established that the first excited PESs ($^1\Pi$) exhibit a collinear barrier of about 2 kcal/mol, but in the case of $S(^1D) + H_2$ it becomes about 10 kcal/mol [11]. Be-

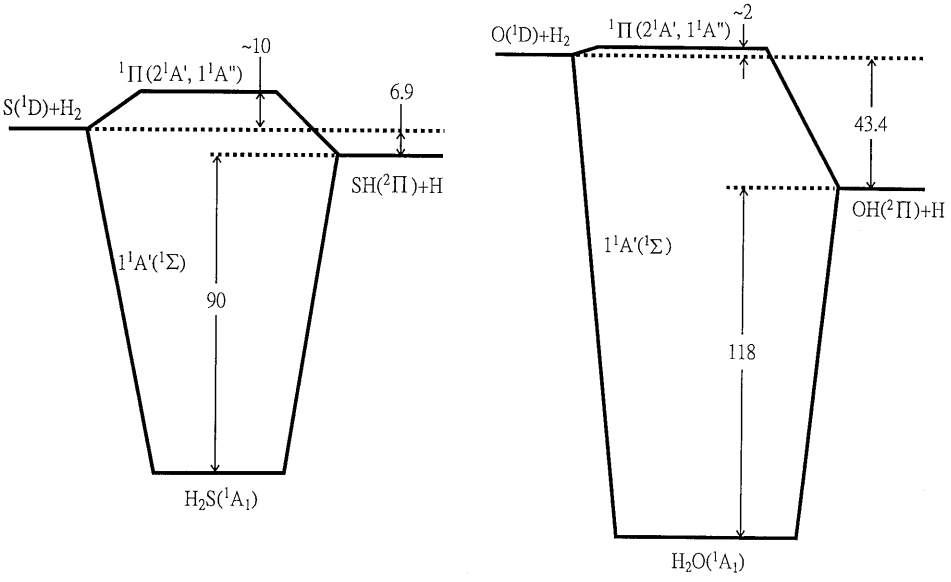

Fig. 1. Schematics of the most relevant energetics for the title reaction and the analogous $O(^1D)$ reaction. Both reactions involve a deep well, yet the exoergicities are very different. The potential barriers on the first excited surface also differ substantially

cause of the relatively low barrier for $O(^1D)+H_2$, the degree of the participation of the $^1\Pi$ surface, which corresponds to a direct abstraction pathway, in total reactivity has recently been at the center of controversy [7, 9, 12–20]. On the other hand, the relatively high barrier of the first excited PESs in $S(^1D)+H_2$ [4, 11] will diminish the abstraction contribution. Hence, the title reaction provides a better opportunity for in-depth exploration of insertion dynamics over a wider energy range.

Such an investigation has recently been undertaken and reported by us for $S(^1D)+D_2$ at two collision energies [2, 6]. The experimental observable was the collision energy dependence of the state-resolved differential cross sections. It was found that the global angular distributions were nearly symmetric, but highly polarized along the forward–backward (f–b) directions. Phase-space theory gave a fair description about product translational energy distribution, but significant discrepancies were noted for angular and the more detailed angle-specific speed distributions. A strong coupling between the product angular and speed distributions was noted. In particular, whereas a pronounced f–b peaking distribution was evident for the SD ($v'=0$) state, a somewhat more isotropic one was revealed for $v'=1$. Reported here is our further attempt to better characterize the detailed dynamics of this prototypical insertion reaction. Section 1 outlines the basic idea of our experimental approach. The experimental results and the comparisons with $S(^1D)+D_2$ are presented in Sect. 2. Conclusions are given in Sect. 3.

1 Experiment

The experiments were carried out in a pulsed, crossed molecular beam apparatus described previously [4, 15, 21]. In brief, a skimmed $S(^1D)$ beam was generated by 193-nm photolysis of CS_2 (0.5% in He, 15 atm.) at the throat of a pulsed valve. The subsequent supersonic expansion confined and translationally cooled the $S(^1D)$ beam which then collided with the target H_2 beam from a second pulsed valve. The detection of the reaction product, H-atom, was achieved by a $(1+1)$ resonance-enhanced multi-photon ionization (REMPI) time-of-flight (TOF) mass spectrometric scheme. The necessary VUV radiation near the H-atom Lyman-α transition (121.6 nm) was generated by the frequency tripling technique in a Kr-gas cell.

To directly map out the desired center-of-mass (c.m.) distribution, the product 3D velocity distribution was interrogated by the Doppler-selected TOF method. This method combines the conventional Doppler-shift and high-resolution ion TOF (in velocity mode) techniques in an innovative manner, and has been detailed previously [15, 22]. Here, only the basic idea is outlined. To measure the three dimensional (3D) velocity distribution of a reaction product, $I(v_x, v_y, v_z)$, the Doppler-shift technique is first applied to selectively ionize a subgroup of products with $v_z \pm \delta v_z$. Rather than collecting all these signals as a single data point in the conventional approach, these Doppler-selected ions are dispersed both spatially (in v_x) and temporally (in v_y). A slit placed in front of the MCP detector restricts only those ions with $v_x \approx 0$ to be detected, and the v_y distribution of those v_x- and v_z-selected ions is then measured by the ion TOF method. Due to the cylindrical symmetry of the product 3D velocity distribution around the initial velocity axis ($\hat{v}_z$) in a crossed-beam scattering experiment, the information about the large v_x distribution will not be lost provided that the parallel configuration (for example, the probe laser propagates along $\hat{v}_z$ for Doppler selection, which is readily achievable with the present rotating-sources machine) is adopted in this approach. Since both the Doppler slice and the ion TOF measurement are essentially in the c.m. frame and the v_x component associated with the c.m. velocity vector is usually small and can be mostly compensated for experimentally, this highly multiplexed measurement yields a direct mapping of the desired c.m. distribution ($d^3\sigma/v^2 dv d\Omega$, expressed in polar coordinates by convention) in a Cartesian velocity coordinate ($d^3\sigma/dv_x dv_y dv_z$). This is to be contrasted with the conventional neutral TOF technique (either in the universal machine [23] or by the Rydberg-tagging approach [24]) for which the laboratory-to-c.m. transformation must be performed, or with the 2D

ion imaging technique [25] which involves a 2D-to-3D back transformation.

2 Results and discussion

2.1 Global view of reaction dynamics

Figure 2a shows typical Doppler profiles of the H-atoms from the title reaction at $E_c = 2.24$ and 3.96 kcal/mol. Whereas the lower energy one (solid dots) shows flat top in shape, a prominent double-hump profile is seen at higher energy (open circles). Also marked in the figure is the location of the c.m. frequency. In both cases, a slight preference for forward-scattered products is discernible. (Note that the direction of the product being detected (H-atom) is referred to the c.m. direction of the reactant H_2 from which the H-atom originates.)

Figure 2b shows a few examples of Doppler-selected TOF spectra. The left (right) panel is for the 2.24 kcal/mol (3.96 kcal/mol) case. The spectra have been converted into velocity space and for clarity only every other data point is shown. Clear steps and fine-structure features are vividly observed, and their appearance and position are sensitive to the initial v_z selection. The Doppler profiles of the H-atom product span over 6 cm^{-1} in width. The TOF measurements were performed for a total of 33 equally spaced Doppler selections to cover the entire profiles. After complications arising from the H-atom Lyman-α doublet were removed [15, 22], the combination of those data together yields the direct mapping of the product 3D velocity distribution. The resulting 3D representations of the velocity-flux contour maps ($d^2\sigma/dvd(\cos\theta)$) for the two collision energies are displayed in Fig. 3. Apparently the contours are quite symmetric, and highly polarized in the forward–backward directions. The degree of polarization becomes more pronounced with the increase in collision energy. Although a nearly symmetric angular distribution for the present reaction can not be regarded as a conclusive evidence for a reaction with long-lived intermediate complex [26], it is entirely consistent with insertion mechanism.

By integrating the doubly differential cross section over the full speed (angle) range for each contour, the product angular distribution $I(\theta) = d\sigma/d(\cos\theta)$ (the product translational energy distribution $P(E_t) = d\sigma/dE_t$) can be obtained. Figure 4 presents the results. The product $P(E_t)$ distributions

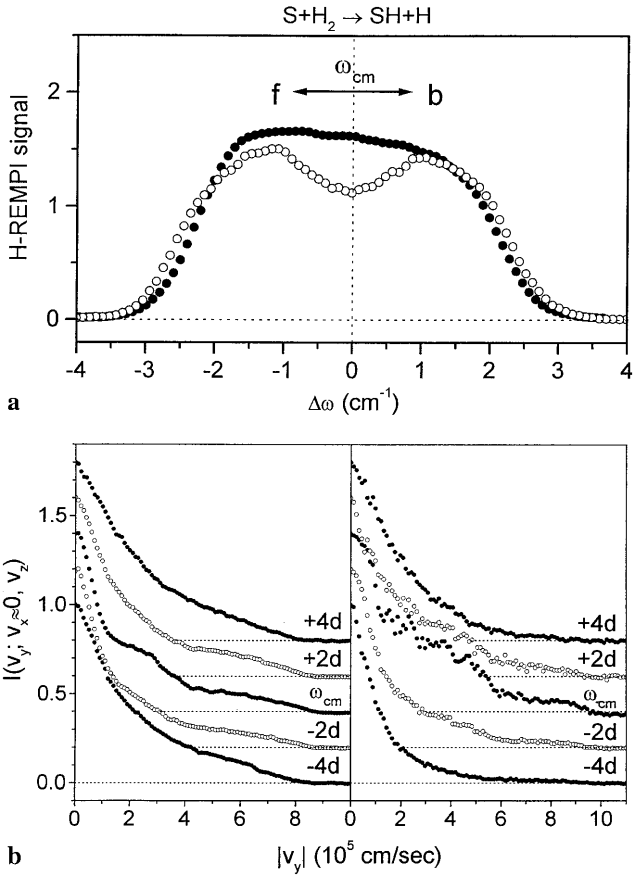

Fig. 2. a Doppler profiles for the title reaction at 2.24 kcal/mol (•) and 3.96 kcal/mol (o), obtained under the parallel configurations. The dotted line marks the partition between the forward (f) and backward (b) hemispheres for the $^2S_{1/2} \rightarrow {}^2P_{3/2}$ transition of the H-atom Lyman-α doublet. **b** A few examples of the Doppler-selected TOF spectra of the H-atom product obtained under the ion extraction field of 1.95 V/cm, the *left* (*right*) panel is for 2.24 kcal/mol (3.96 kcal/mol). The label "ω_{cm}" corresponds to the VUV laser frequency that slices through the Newton sphere near c.m., and each "*d*" corresponds to 0.365 cm^{-1} in frequency or $v_z = 1.335 \times 10^5$ cm/s

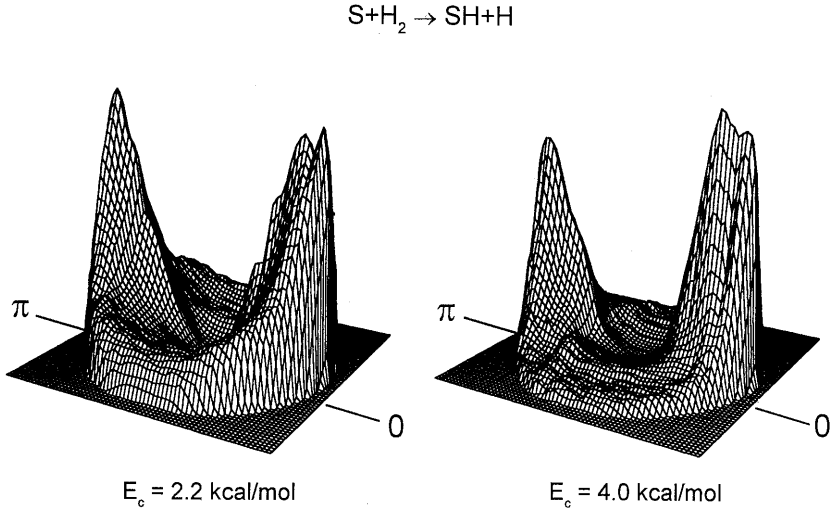

Fig. 3. The 3D representation of the H-atom velocity-flux contour, $d^2\sigma/dvd(\cos\theta)$. The contours are constructed directly from a total of 33 slices of the Doppler-selected TOF measurements

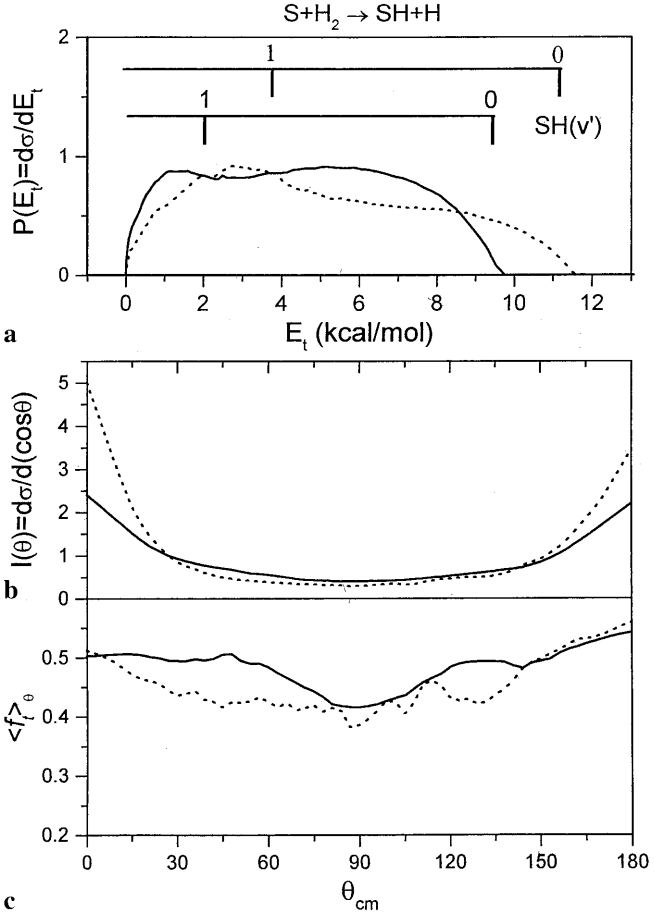

Fig. 4a–c. The product translational energy distributions $P(E_t) = d\sigma/dE_t$ (**a**), the product c.m. angular distributions $d\sigma/d(\cos\theta)$ (**b**), and the fractions of the average translational energy release (**c**) for 2.24 kcal/mol (*solid lines*) and 3.96 kcal/mol (*dashed lines*). Also marked in **a** is the onset of the vibrational state of the SH product

are rather broad at both collision energies, and the vibrational structures are also apparent as can be compared with the stick marks shown on top. The angular distributions are fairly symmetric. Both the slight forward-preference at the two energies and the more polarized distribution at higher collision energy, as noted early, are readily observed. In terms of the fraction of the average translational energy release, $\langle f_t \rangle$, a small variation with the c.m. scattering angle can be seen. This quantity, $\langle f_t \rangle_\theta$, gives a quantitative measure of the coupling of the product angular and speed distributions. Compared to the previously reported $S(^1D) + D_2$ [2, 6], this coupling appears to be weaker for the present reaction. Nevertheless, the angle-integrated fractions of kinetic energy release are 0.48 and 0.45 for $E_c = 2.24$ and 3.96 kcal/mol, respectively, which are quite comparable to the $S(^1D) + D_2$ cases (within a few percent).

2.2 Angle- and state-specific analysis

A more informative way to reveal the detailed dynamics afforded by this direct 3D mapping approach is to examine the angle-specific kinetic energy distribution $P(E_t; \Delta\theta)$ over a limited range of $\Delta\theta$. The results for the two energies are presented in Fig. 5. For convenience, they are displayed as a function of $E_{int} = E_{total} - E_t$ through energy conservation such that the energetic marks shown in the 0–15° panel apply to all other panels and for both collision energies. Several interesting observations are worth noting.

First, the products scattered in different angles clearly display different internal energy distributions. That is a manifestation of the coupling between angle and speed distributions as alluded to early. Similar findings were noted for the $S(^1D) + D_2$ reaction [6]. Second, whereas the global angular distributions are fairly symmetric at both collision energies, the detailed $P(E_{int}; \Delta\theta)$ distributions behave differently for the two cases. At $E_c = 2.24$ kcal/mol, the f–b symmetry is roughly retained, for example comparing the shape of $P(E_{int})$ at 0–15° to that at 165–180°. At slightly higher energy of 3.96 kcal/mol, such a f–b symmetry apparently breaks down. This is in constrast with the $S(^1D) + D_2$ reaction for which both the 2.3 and 5.3 kcal/mol cases display a rough f–b symmetry in terms of the angle-specific energy distributions. Third, the vibrational structures in most of the panels can readily be identified by inspections of the $P(E_{int})$ shape in each panel with respect to the energetic onsets for SH(v'). Since the $P(E_{int})$ distributions at two energies have been normalized to their integral cross sections [4], it becomes apparent that with the increase in collision energy, there is a dramatic variation in product state distributions and this variation depends sensitively on scattering angles. This is again at variance with the behavior found previously for $S(^1D) + D_2$, which showed a rather uniform variation for different angles. Furthermore, some distinct fine structures near sideward direction (where the present mapping technique has higher resolution in translational energy) are seen, which correspond to partially-resolved (high-j') rotational states of the SH($v' = 0$) products. Due to limited resolution of this work and the complication of energy level structures of the open-shell species ($SH(^2\Pi)$), a definite assignment of these rotational structures can not be made.

These qualitative observations can be put forward semi-quantitatively through product state analysis. Figure 6 illustrates the vibrational state partitioning for three angular segments. A parameterized form was assumed for the product rotational state distribution for a given v' in this partition. The parameters were varied and the finite experimental resolution was convoluted for the best fit of each angle-specific kinetic energy release distribution. Although such a partitioning is never unique, the essential features described below remain unaltered. It is interesting to note that although the rotational envelopes for $v' = 0$ are broad in all cases, those in the f–b directions display distinct bimodal distributions which are absent for the sideward-scattered products. No clear sign of a bimodal rotational distribution was observed in our previous $S(^1D) + D_2$ studies. Since no statistical theory will predict a bimodal rotational distribution, it implies the presence of some "hidden" dynamical factors in this reaction. Figure 7 summarizes the resultant angle-specific energy disposal and the vibrational branching. Consider first the angle-integrated quantities (the corresponding numbers in parentheses). Both the energy disposal and the vibrational branching are in good agreement with simple statistical expectations. For example, the experi-

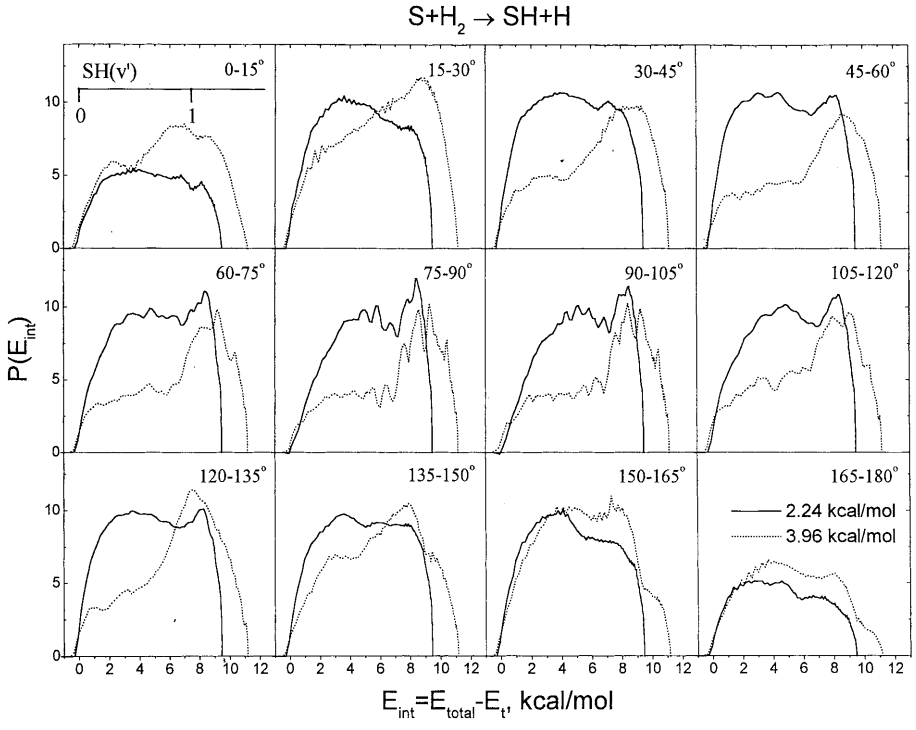

Fig. 5. Angle-specific internal energy distribution of the SH product over every 15° angular segment. The results for the two energies have been normalized to their integral cross sections [4]. The energetic onset for SH(v') is shown only for 0–15°, though it applies to all other angular ranges

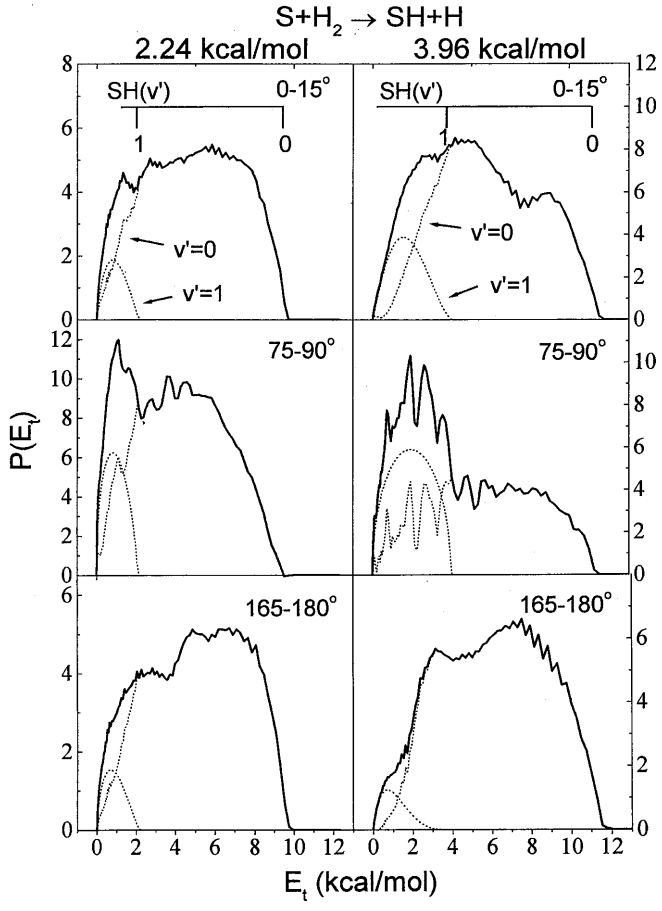

Fig. 6. Partition of the angle-specific translational energy distributions into the SH vibrational states, exemplified by three different angular segments for each case. Note the bimodal features for SH($v' = 0$). Since the separation of spin-orbit manifolds for SH($^2\Pi$) is only 1.08 kcal/mol, these bimodal features can not be ascribed to being electronical fine-structure in nature

mental $P_{v'} = 0 : P_{v'} = 1$ branchings are 0.91:0.09 for E_c = 2.24 kcal/mol and 0.83:0.17 for 3.96 kcal/mol, which compare with the statistical values of 0.92:0.08 (2.24 kcal/mol) and 0.85:0.15 (3.96 kcal/mol). The statistical theory predicts a slightly larger (smaller) value for translational (rotational) energy disposal than experiment. But, the discrepancies are only a few percent.

The situation becomes quite intriguing in terms of the angle-specific reaction attributes. As is seen, the sideward-scattered products clearly exhibit more vibrational excitation than those in the f–b directions, and this disparity becomes more pronounced with the increase in E_c. Similar features were found for the $S(^1D) + D_2$. In our previous report on $S(^1D) + D_2$ [2], a similar angular variation for translational energy disposal was seen and compared with a phase-space theory (PST) calculation [27]. It was shown there that in PST such an angular pattern for translational energy disposal is a result of a purely kinematic requirement imposed by the angular momentum conservation. In other words, the smaller translational energy disposal for sideward-scattered products should be compensated by a larger disposal into rotation, not vibration, in sideways if it is purely kinematic in origin. These observations suggest that different types of complexes and/or mechanisms might be involved for producing different vibrational states of SH/SD. A conjecture that lies on the correlation between the initial impact parameter and the type of complex was proposed [2]. Theoretical investigation along this line is currently in progress.

The shape of the vibrational "band" exemplified in Fig. 6 also contains the information about the product rotational distribution. The recoil energy E_t and the product rotational energy E_r for vibrational state v' are related by $E_t = E_{total} - E_{v'} - E_r$. Because of the complication from the open-shell energy level structure and of the limited resolution of this work,

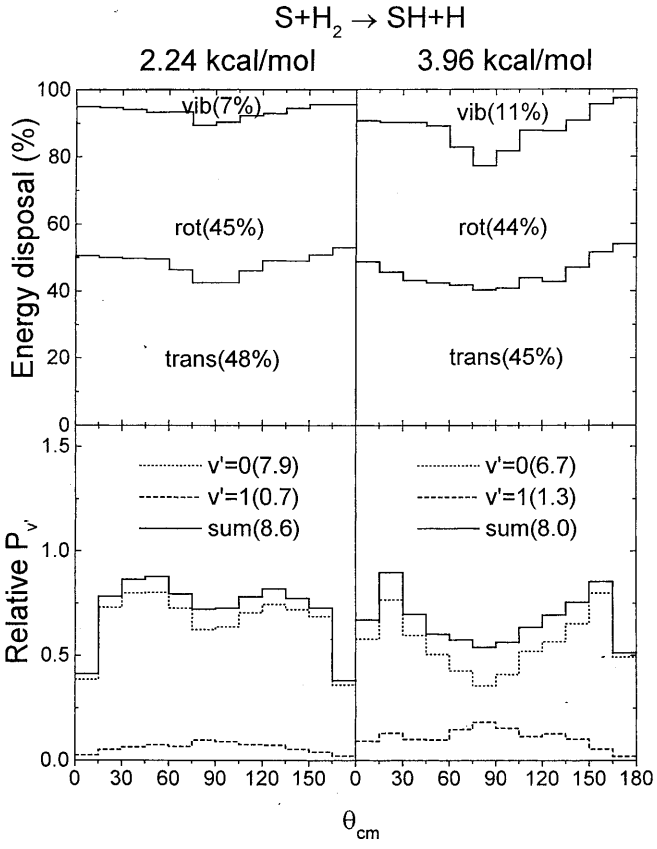

Fig. 7. Summary of the angle-specific energy disposal and the angle-specific vibrational branching for the two energies. The numbers in parentheses give the corresponding angle-integrated values

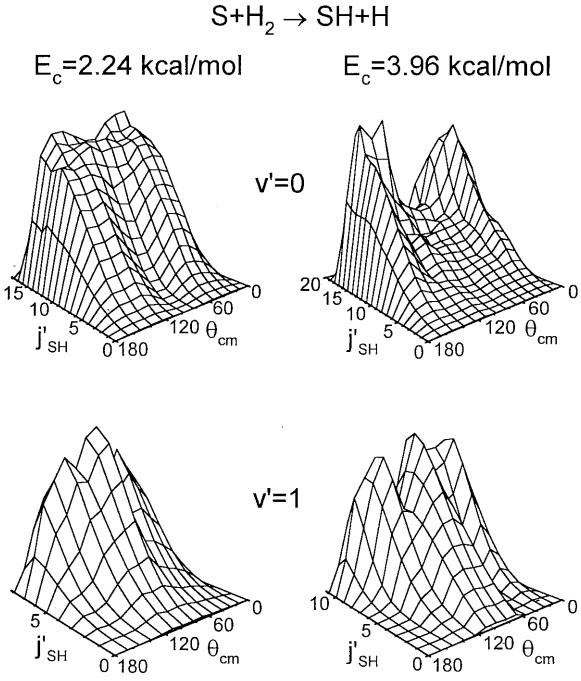

Fig. 8. The 3D representation of the gross features of product rovibrational state-specific angular distributions ($d\sigma_{v'j'}/d\theta$). For clarity, the four panels are not normalized to one another

only the main features in rotational distributions are sought here. Thus at a fixed c.m. angle, the "classical" rotational state distribution is

$$P(j') = P(E_t)\,dE_t/dj' = 2B_{v'}(j'+1/2) \times P[E_{total} - E_{v'} - B_{v'}j'(j'+1)] \quad (1)$$

where $B_{v'}$ is the rotational constant for the vibrational state v'. Figure 8 summarizes the results which show how the rotational state distributions for different vibrational states vary with the c.m. angles, and how they vary with the initial collision energies. Although all cases display a high degree of rotational excitations, the detailed contours are different. Note that due to the $\sin\theta$ term in the integration over all azimuthal angles, an isotropic angular distribution, for example, $d\sigma/d(\cos\theta) =$ constant, will appear as sideward peaking in the $d\sigma/d\theta$ representation. And a flat-top $d\sigma/d\theta$ distribution will turn into a f–b peaking distribution in the conventional $d\sigma/d(\cos\theta)$ representation for angular distribution. Now let us first examine the 2.24 kcal/mol case. For $v' = 0$, the actual angular distributions all appear to be f–b peaking and the degree of polarization is more pronounced for smaller $j's$ than for the larger ones. By way of contrast, for $v' = 1$ the angular distribution becomes much less polarized; in fact, it shows the tendency towards an isotropic one. For a reaction which forms an intermediate complex, the exact shape of the c.m. angular distribution of products reflects the propensity in angular momentum disposal [28]. In simple terms, a f–b peaking angular distribution corresponds to $\boldsymbol{L} \approx \boldsymbol{L}'$ and an isotropic distribution implies $\boldsymbol{L} \approx \boldsymbol{j}'$. It is quite remarkable that both extreme types of directional correlation in angular momentum disposal are revealed here for different vibrational states in the very same reaction. With the increase in E_c (3.96 kcal/mol) the degree of alignment of $\boldsymbol{L}'$ to $\boldsymbol{L}$ becomes even more pronounced for $v' = 0$, presumably reflecting the smaller value of maximal impact parameter (i.e., smaller value for $\boldsymbol{L}_{max}$) at higher collision energies – a typical behavior for a barrierless capture reaction. For $v' = 1$, while low $j's$ remain nearly isotropic, a richer angular distribution is seen for the higher $j's$. Its origin remains unclear.

3 Conclusions

The doubly differential cross sections $d^2\sigma/dvd(\cos\theta)$ for the reaction $S(^1D) + H_2$ at 2.24 and 3.96 kcal/mol were mapped out by a newly developed technique called Doppler-selected TOF method. The resolution of this method is sufficiently high to observe directly the product vibrational structures and to infer the main features of the rotational energy distributions. Detailed comparisons were made as to their dependences on the initial collision energies for this reaction, as well as with those for the $S(^1D) + D_2$ reaction. It was found that the global attributes such as the energy disposal, vibrational branching and total angular distribution of these two isotopically analogous reactions are quite similar. They all show characteristic features of a complex-forming reaction, and can readily be understood by statistical arguments. The more detailed reaction attributes, however, display significant differences and subtleties, most notably the angular variation in product vibrational excitation and the bimodal rotational distributions in the f–b directions, which can not be reconciled on statistical grounds. Apparently there is

rich dynamical information underneath the statistical treatment to be uncovered for an indirect complex-forming reaction. These subtle dynamical factors are often hidden or washed out upon the averaging over the scattering angles. As exemplified in this work, angle-specific distributions provide a vehicle to decode the underlying dynamics from the statistical factors. We hope that the work presented here will provide the stimulus for future theoretical investigations and for better understanding of insertion reactions in general.

Acknowledgements. This work was supported by the National Science Council of Taiwan and by the Chinese Petroleum Corporation.

References

1. R.D. Levine, R.B. Bernstein: *Molecular Reaction Dynamics and Chemical Reactivity* (Oxford University Press, Oxford 1987)
2. S.-H. Lee, K. Liu: J. Phys. Chem. **102**, 8637 (1998)
3. M.S. Fitzcharles, G.C. Schatz: J. Phys. Chem. **90**, 3634 (1986)
4. S.-H. Lee, K. Liu: Chem. Phys. Lett. **290**, 323 (1998); Erratum **317**, 516 (2000)
5. Y. Inagaki, S.M. Shamsuddin, M. Kawasaki: Laser Chem. **14**, 108 (1994)
6. S.-H. Lee, K. Liu: *In Advances in Molecular Beam Research and Applications*, ed. by R. Campargue (Springer, Berlin 2000)
7. Y.-T. Hsu, J.-H. Wang, K. Liu: J. Chem. Phys. **107**, 2351 (1997)
8. G.G. Balint-Kurti, A.I. Gonzalez, E.M. Goldfield, S.K. Gray: Faraday Discuss. **110**, 169 (1998)
9. G.C. Schatz, A. Papaioannou, L.A. Pederson, L.B. Harding, T. Hollebeek, T.-S. Ho, H. Rabitz: J. Chem. Phys. **107**, 2340 (1997)
10. A.J. Dobbyn, P.J. Knowles: Mol. Phys. **91**, 1107 (1997)
11. D. Simah, B. Hartke, H.-J. Werner: J. Chem. Phys. **111**, 4523 (1999); A. Mebel: private communication.
12. G.C. Schatz, L.A. Pederson, P.J. Kuntz: Faraday Discuss. **107**, 357 (1997)
13. K. Drukker, G.C. Schatz: J. Chem. Phys. **111**, 2451 (1999)
14. S.K. Gary, C. Petrongolo, K. Drukker, G.C. Schatz: J. Phys. Chem. **103**, 9448 (1999)
15. Y.-T. Hsu, K. Liu, L.A. Pederson, G.C. Schatz: J. Chem. Phys. **111**, 7921 and 7931 (1999)
16. M. Alagia, N. Balucani, L. Cartechini, P. Casavecchia, E.H. van Kleef, G.G. Volpi, P.J. Kuntz, J.J. Sloan: J. Chem. Phys. **108**, 6698 (1998)
17. M. Ahmed, D.S. Peterka, A.G. Suits: Chem. Phys. Lett. **301**, 372 (1999)
18. A.J. Alexander, F.J. Aoiz, M. Brouard, J.P. Simons: Chem. Phys. Lett. **256**, 561 (1996)
19. A.J. Alexander, D.A. Blunt, M. Brouard, J.P. Simons, F.J. Aoiz, L. Banares, Y. Fujimura, M. Tsubouchi: Faraday Discuss. **108**, 375 (1997), and references therein
20. F.J. Aoiz, L. Banares, V.J. Herrero: Chem. Phys. Lett. **310**, 277 (1999)
21. R.G. Macdonald, K. Liu: J. Chem. Phys. **91**, 821 (1989)
22. J.-H. Wang, Y.-T. Hsu, K. Liu: J. Phys. Chem. **101**, 6593 (1997)
23. Y.T. Lee: Science **236**, 680 (1987)
24. L. Schnieder, K. Seekamp-Rahn, E. Wrede, K.H. Welge: J. Chem. Phys. **107**, 6175 (1997)
25. A.J.R. Heck, D.W. Chandler: Ann. Rev. Phys. Chem. **46**, 355 (1995)
26. R.J. Buss, P. Casavecchia, T. Hirooka, S.J. Sibener, Y.T. Lee: Chem. Phys. Lett. **82**, 386 (1981)
27. R.A. White, J.C. Light: J. Chem. Phys. **55**, 379 (1971)
28. W.B. Miller, S.A. Safron, D.R. Herschbach: Discuss. Faraday Soc. **44**, 108 (1967)